Available online at www.sciencedirect.com
SCIENCE DIRECT®
International Journal of Solids and Structures 42 (2005) 517–538
INTERNATIONAL JOURNAL OF SOLIDS and STRUCTURES
www.elsevier.com/locate/ijsolstr

Effect of a nonuniform distribution of voids on the plastic response of voided materials: a computational and statistical analysis

Nicolas Bilger [a,b,c,*], François Auslender [a], Michel Bornert [a], Jean-Claude Michel [b], Hervé Moulinec [b], Pierre Suquet [b], André Zaoui [a]

[a] *Laboratoire de Mécanique des Solides, École Polytechnique, CNRS, 91128 Palaiseau Cedex, France*
[b] *Laboratoire de Mécanique et d'Acoustique, CNRS, 13402 Marseille Cedex 20, France*
[c] *Électricité de France, Site des Renardières, Route de Sens, Écuelles, 77818 Moret sur Loing, France*

Received 13 April 2004; received in revised form 14 June 2004
Available online 26 August 2004

Abstract

This study investigates the overall and local response of porous media composed of a perfectly plastic matrix weakened by stress-free voids. Attention is focused on the specific role played by porosity fluctuations inside a representative volume element. To this end, numerical simulations using the Fast Fourier Transform (FFT) are performed on different classes of microstructure corresponding to different spatial distributions of voids. Three types of microstructures are investigated: random microstructures with no void clustering, microstructures with a connected cluster of voids and microstructures with disconnected void clusters. These numerical simulations show that the porosity fluctuations can have a strong effect on the overall yield surface of porous materials. Random microstructures without clusters and microstructures with a connected cluster are the hardest and the softest configurations, respectively, whereas microstructures with disconnected clusters lead to intermediate responses. At a more local scale, the salient feature of the fields is the tendency for the strain fields to concentrate in specific bands. Finally, an image analysis tool is proposed for the statistical characterization of the porosity distribution. It relies on the distribution of the 'distance function',

* Corresponding author. Address: Laboratoire de Mécanique des Solides, École Polytechnique, CNRS, 91128 Palaiseau Cedex, France. Tel.: +33 1 69 33 33 70; fax: +33 1 69 33 30 26.
E-mail addresses: bilger@lms.polytechnique.fr (N. Bilger), auslende@lms.polytechnique.fr (F. Auslender), bornert@lms.polytechnique.fr (M. Bornert), michel@lma.cnrs-mrs.fr (J.-C. Michel), moulinec@lma.cnrs-mrs.fr (H. Moulinec), suquet@lma.cnrs-mrs.fr (P. Suquet), zaoui@lms.polytechnique.fr (A. Zaoui).

0020-7683/$ - see front matter
doi:10.1016/j.ijsolstr.2004.06.048

the width of which increases when clusters are present. An additional connectedness analysis allows us to discriminate between clustered microstructures.

Keywords: Porous media; Plasticity; Porosity distribution; FFT calculations; Microstructures

1. Introduction

An accurate description of the effective behavior of porous materials is required to model accurately the ductile fracture of materials. Since the pioneering work of Gurson (1977), whose celebrated criterion was derived from the analysis of a rigid perfectly plastic hollow sphere, a number of studies have led to various improvements of this criterion. Most of them are based on the analysis of a unit-cell consisting of a unique (generally spherical) void surrounded by a cylindrical block of nonlinear matrix subjected to periodic boundary conditions. Tvergaard and Needleman introduced several modifications in Gurson's model to better fit unit-cell computations leading to the Gurson–Tvergaard–Needleman (GTN) model (see Tvergaard, 1990 for a review). First a multiplicative factor q_1 for the porosity has been introduced to model the influence of interactions between voids on the effective yield surface of porous materials. Then, in order to capture the acceleration of the cavity growth near coalescence, the actual porosity f has been replaced by an effective larger porosity f^*. In a subsequent work, also based on the Finite Element Method, Koplik and Needleman (1988) showed that the response of a voided axisymmetric unit-cell can be accurately reproduced by the GTN criterion. They also observed that beyond a critical value of the macroscopic equivalent strain, the local strain field localizes between neighboring voids. Other treatments of the cavity growth and coalescence can be found in Thomason (1990) and Leblond and Perrin (1999) among others. Gurson's criterion has also been extended to account for changes in pore shape by considering spheroidal voids subjected to a macroscopic stress parallel to one of their axes (Gologanu et al. (1993) for ideally plastic materials, Gărăjeu and Suquet (1997) for viscoplastic and ideally plastic material), and to anisotropic matrices obeying an orthotropic quadratic Hill criterion (Benzerga et al., 1999).

Despite the progress that has been made, the analytical models available so far are still unable to take into account the actual spatial distribution of the voids or, at least, the fluctuations in local porosity on both the overall and local responses of voided materials. Becker (1987) has performed two-dimensional finite element simulations for an elastic–viscoplastic material obeying the GTN criterion with an inhomogeneous porosity distribution. His results show that the plastic flow concentrates into bands in areas with large void volume fraction, resulting in local failure by coalescence between these bands. In an analytical study, Perrin and Leblond (1990) have considered a composite sphere composed of two porous plastic materials each of them obeying Gurson's criterion with its own porosity. They found that, under hydrostatic stress, the macroscopic yield stress is different from the one derived for the average homogeneous porosity, showing an effect of the porosity distribution on the effective yield properties of voided materials. Distribution effects in porous media or in metal matrix composites have been investigated by many authors by means of finite element simulations (Brockenbrough et al., 1991; Böhm and Rammerstorfer, 1995; Soppa et al., 1998). Most of these studies rely on simulations of periodic microstructures with unit cells containing only a limited number of pores or reinforcements, which can hardly mimic realistic situations of random media. Very local interactions between neighboring inclusions or pores of similar or different sizes can be studied in this way, but the investigation of long range interactions governed by the statistics of an actual random distribution, requires large scale simulations which are often limited by computer capabilities. This is why most investigations are often limited to two-dimensional analyses. These computations show however that strain localization phenomena under uniaxial tension are strongly dependent on distri-

bution effects (Soppa et al., 1998). More general loading conditions for two-dimensional porous media under finite strain have recently been investigated by Pijnenburg and Van der giessen (2001) but only one pore unit cells have been considered. Significant deviations of the effective response of such porous media with respect to Gurson's model have been observed and they seem to be associated with a strong localization of the local strain field, especially for nonaxisymmetric loading conditions. Interactions between pores of different sizes have been investigated in the context of classical plasticity by Faleskog and Shih (1997) and Pardoen and Hutchinson (2003) or in the framework of nonlocal plasticity by Tvergaard and Niordson (2004). Once again the considered pore distributions were very regular when not perfectly periodic. The plastic response of a porous material made up of a more realistic microstructure accounting for a nonuniform distribution of cylindrical voids (without clusters) has recently been investigated numerically by Michel et al. (2001). In this work, the matrix was ideally plastic, satisfying periodic boundary conditions and subjected to an axisymmetric loading in the direction of the cylindrical void. An algorithm based on the fast Fourier transform (FFT) was preferred to finite element simulations to handle the large numbers of degrees of freedom required in these calculations. In opposition to previous works, the size of the unit-cell was much larger than the pore size (about 30 times larger) so that a larger variability in the relative position of neighboring pores could be taken into account in the simulations. In addition, the computations are expected to be less sensitive to the periodic boundary conditions which are used. The results showed significant effects of the distribution on the yield surface. In particular, the yield stress at high triaxiality is significantly reduced. In addition, in agreement with previous observations by Becker, they found that the deformation tends to concentrate into bands linking voids to form a path through the representative volume element (RVE). These results suggest that a systematic study of the effects of the porosity distribution on the global and local response of porous materials is of definite interest. This is the main goal of this paper.

The first part of the paper is devoted to the different types of microstructures investigated in this study, representing random distributions of voids with or without clusters. Within the class of clustered microstructures there exist two different sub-classes according to whether the clusters are connected to each others or disconnected.

In the second part of the paper, two-dimensional and three-dimensional FFT simulations are performed on such microstructures for different loading conditions and different triaxiality ratios ranging from purely hydrostatic stress to pure shear stress. The results show that the porosity distribution has an effect on the yield stress, the importance of which depends on the type of microstructure: microstructures without clusters exhibit the highest yield stress, microstructures with connected clusters are the softest ones whereas microstructures with disconnected clusters show intermediate responses. These general trends hold irrespective of the directions and of the intensity of the macroscopic stress but the amplitude of the deviations does depend on those factors. Furthermore, as found in Becker (1987) and in Michel et al. (2001), the deformation tends to concentrate in bands linking the voids together to form a path through the RVE.

Finally, because of the strong influence of the type of microstructures on the macroscopic and microscopic behavior of the porous media that has been found, we propose a statistical tool to detect the presence of clusters in a porous microstructure. It is based on the "distance function" giving at each point in the matrix the distance to the nearest pore. In addition, an analysis of the connectedness of the clusters is proposed to distinguish microstructures with connected clusters from those with disconnected clusters.

2. Simulation of microstructures

Currently available computational codes can hardly be used to perform systematic investigations of representative microstructures obtained from real samples. In addition, in order to obtain generic results which do not depend on the specific details of a given microstructure, it is more appropriate to perform numerical

simulations on microstructures which obey some known statistical properties (a detailed exposition of the statistics of random microstructures can be found in Torquato (2003)). This is why *simulated microstructures* or RVE's were used in this study. They consist of a homogeneous matrix containing circular or spherical voids. Two main families were generated: "random" microstructures where no particular clustering effect is enforced and "clustered" microstructures where either connected or disconnected clusters are deliberately introduced.

2.1. Random microstructures

Several schemes can be used to generate random microstructures. Spherical (for three-dimensional simulations) or circular (for two-dimensional ones) voids, defined by the coordinates of their center and their radius, are implanted according to a point process for the coordinates and to a random scalar process for the radius. Depending on the assumptions made for the implementation of the voids, different types of microstructures are obtained as shown in Fig. 1. In the classical Boolean model, the centers are randomly implanted according to a standard Poisson process, with no limitation on their relative positions, so that the voids can overlap (Fig. 1a). A constraint on the minimal distance between voids can be imposed to prevent void overlapping. This distance is zero for the hard sphere model (Fig. 1b) and is strictly positive for the cherry pit model (Fig. 1c) where voids can neither overlap nor come into contact (Torquato, 2003). In both latter cases, pores are generated one after the other: if the current pore does not satisfy the minimal distance requirement, it is removed and a new one is generated until the distance condition is fulfilled. The pore size can be the same for all voids or different; in the second case a uniform probability law for the pore size distribution has been adopted. The overall porosity can be monitored precisely. In the case of a single pore size (monodisperse case) the radius is derived from the described porosity and the total number of pores (about 40) and from the known volume (or area) of the RVE. In the polydisperse case new pores are added as long as the prescribed porosity is not exceeded; as soon as it is, the radius of the last void is reduced until the prescribed porosity is reached. Note that a precise porosity is required for comparison purposes: since the overall behavior is strongly dependent on the pore volume fraction, morphological effects related to pore distribution need to be investigated at the same porosity.

The computational method used here requires the unit-cells to be periodic. In the case of hard spheres or cherry pits, the constraint on the minimal distance between voids is to be imposed not only between voids located inside the unit-cell itself (main unit-cell) but also to voids located in the N cells ($N = 26$ in three dimensions, $N = 8$ in two dimensions) adjacent to the main one. When a void intersects one of the edges of the main unit-cell and then falls partly into the peripheral cells, it is split into two or four parts in the

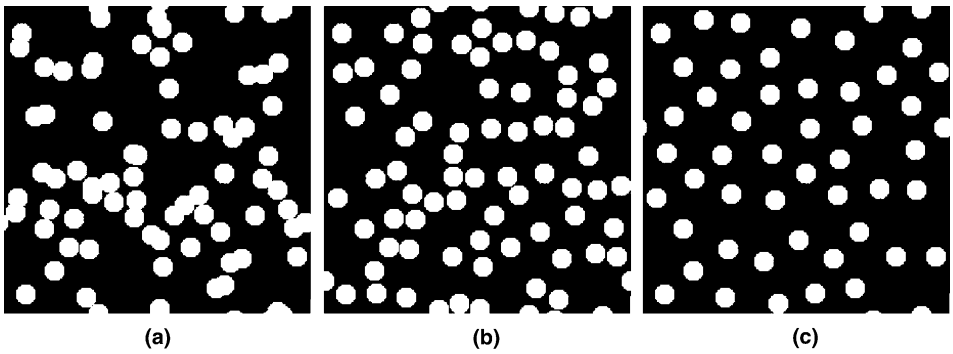

Fig. 1. Two-dimensional random periodic microstructures with identical size: (a) classical boolean model; (b) hard sphere model and (c) cherry pit model.

two-dimensional case or into 2, 4 or 8 parts in the three-dimensional case. The parts belonging to the main unit-cell stay in place whereas the parts falling in the peripheral cells are moved into the main unit-cell by periodicity.

2.2. Clustered microstructures

A two-step procedure is used to generate clustered microstructures. The coarser scale is associated with the clusters whereas the finer scale is associated with the voids themselves.

A two-scheme process is used to generate two microstructures with very different sphere radii, say 'small' and 'large' spheres, which are then superimposed. If only the 'small' voids with centers belonging to the 'larger' spheres are retained, a clustered microstructure with disconnected clusters is obtained. Conversely, if the 'small' voids with centers outside the larger spheres are retained, a clustered microstructure with connected clusters is obtained. Note that in the realizations of the clustered microstructures that have been considered in this study, the connected clusters are all connected to each others, so that there is only one single connected cluster in the RVE. Example of such two-dimensional microstructures derived from the cherry pit model used for both scales with variable void sizes is given in Fig. 2.

The total volume fraction of these clustered microstructures has again to be monitored precisely and the following procedure has been adopted. First a microstructure with large spheres (or disks) is generated as already described. A second process with smaller pores is then considered in association with the chosen minimal distance condition but now only the voids located inside the larger spheres of the first process are retained. The total porosity may then be obtained by adding pores until the prescribed porosity is reached and by adjusting the size of the last pore (polydisperse case), or by adding pores until the required number of pores is attained (uniform pore size).

It is not possible to reach large pore volume fraction with such simple incremental procedures for the pore implementation, especially in the case of clustered cherry pit models, since, over a critical volume fraction, it becomes impossible to insert additional pores due to the lack of space between existing pores. More sophisticated procedures by which existing pores can be moved have been developed (Torquato, 2003). In the present study where the void volume fraction is less than a few percents, it has not been necessary to resort to these more elaborate algorithms.

Once the pore centers and radii are generated, a binary image of the unit cell required for further use in the FFT calculations is created at a spatial resolution (number of pixels or voxels) prescribed by the user. Black pixels correspond to the matrix and white ones to the pores. Because of the discrete nature of the image and of the unavoidable rounding off errors it induces, the final volume fraction of the images, given

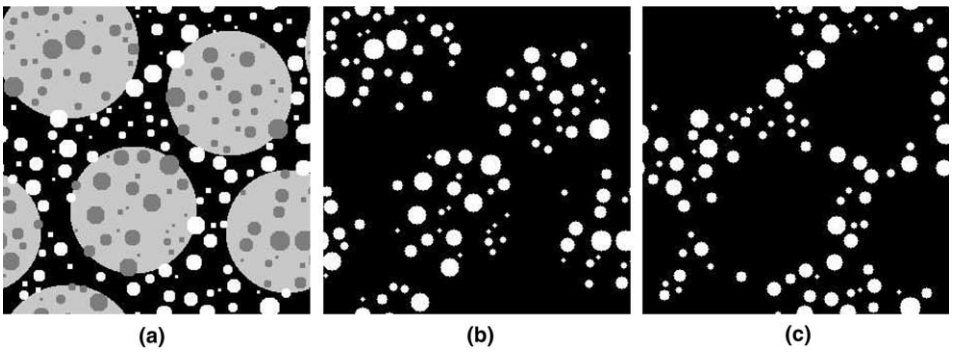

Fig. 2. Periodic clustered microstructures resulting from two cherry pit processes: (a) Superposed cherry pit schemes; (b) disconnected clusters and (c) connected clusters.

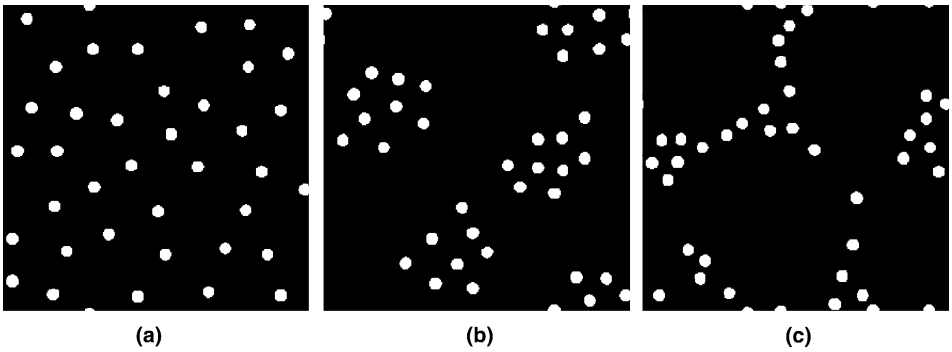

Fig. 3. Simulated periodic microstructures: (a) cherry pit random process; (b) disconnected clusters and (c) connected clusters. $f_s = 4.6\%$, uniform pore size.

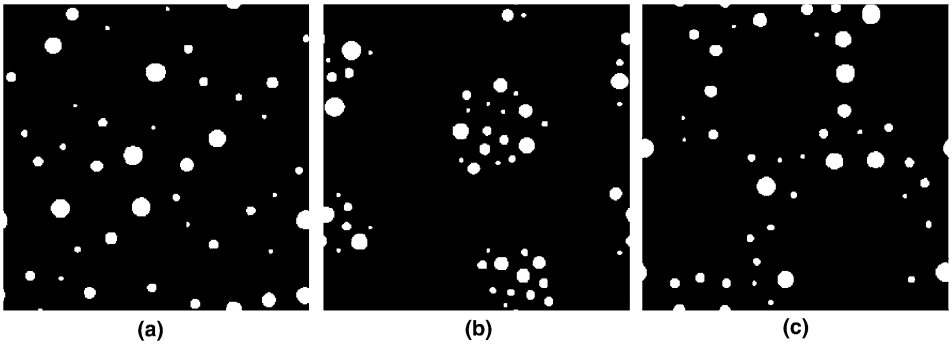

Fig. 4. Simulated periodic microstructures: (a) cherry pit random process; (b) disconnected clusters and (c) connected clusters. $f_s = 4.6\%$, nonuniform pore size.

by the ratio of white pixels to the total number of pixels, might slightly differ from the prescribed volume fraction, but never by more than 0.03%.

Figs. 3 and 4 show the three types of two-dimensional periodic microstructures used in the FFT computations. Each type of microstructure has two variants: the first with uniform pore sizes—one for the pores and one for the clusters—and the second with a variable size for the pores. All six microstructures have the same macroscopic porosity equal to 4.6%. They were generated with the cherry pit scheme for both scales. Specific values of the pore and cluster radii are given in Table 1. These values are given for a cell with a length equal to 1. Fig. 5 shows the same three types of periodic microstructures obtained with the cherry pit three dimensional scheme with a uniform void radius equal to 0.033 for the pores and to 0.19 for the clusters. The minimal distance between pores and clusters is given in Table 1 and the overall porosity is 0.6% for each three-dimensional microstructure.

The microstructures presented in Figs. 3–5 are examples of those that actually served for the FFT calculations. Since the number of pores is large and their size is small with respect to the cell size, the realization of the random microstructures is expected to be more representative of an actual material than simulations based on periodic microstructures with only a couple of pores. However, the realizations for clustered microstructures contain only four clusters and can thus hardly be considered as statistically representative of real microstructures with a random distribution of clusters. Considering a large number of clusters would lead to huge images which are beyond currently available computer capabilities. To over-

Table 1
Parameters used for the generation of the microstructures shown in Figs. 3–5

Microstructure	Pore size (radius)	Min. dist. between pores	Cluster size (radius)	Min. dist. between clusters	Void volume fraction (%)
3a	0.01953	0.08	–	–	4.6
3b	0.01953	0.04	0.215	0.15	4.6
3c	0.01953	0.01	0.3	0.04	4.6
4a	0.005 to 0.035	0.08	–	–	4.6
4b	0.005 to 0.035	0.04	0.215	0.15	4.6
4c	0.005 to 0.035	0.01	0.30	0.04	4.6
5a	0.033	0.18	–	–	0.6
5b	0.033	0.03	0.22	0.20	0.6
5c	0.033	0.08	0.36	0.04	0.6

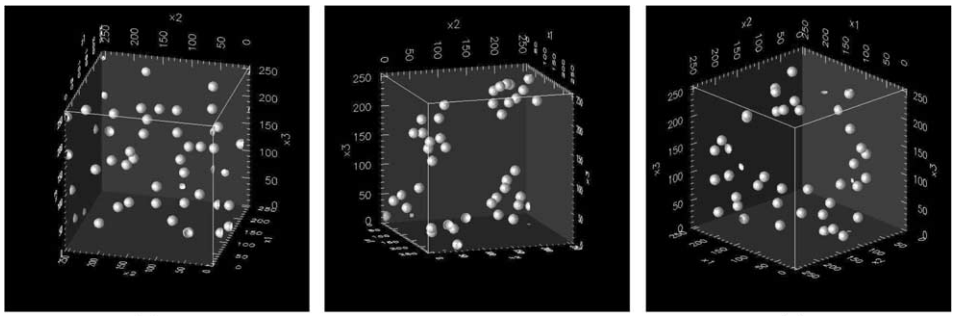

Fig. 5. Periodic three-dimensional clustered microstructures with uniform pore size: (a) random; (b) disconnected clusters and (c) connected cluster.

come this difficulty, several computations have been performed on different realizations of the microstructure corresponding to the same (limited) statistical information. In practice, four or five realizations have been considered for each set of data and the corresponding results have been averaged. The dispersion of the results from one configuration to another will be discussed. Admittedly it would have been preferable to consider more realizations and this limited number was mostly motivated by computer limitations: some of the three-dimensional simulations took more than one week on a multiprocessor workstation.

A more thorough analysis of the results shows in addition that the number of realizations that were used in the present study, even limited, might be sufficient to reach a stable value for the ensemble average of the results and to draw at least qualitative conclusions from these ensemble averages. Indeed, the dispersion of the results between all realizations of a given microstructure provides a mean to qualitatively evaluate the representativity of the results. It turns out that the results obtained with random porous media are less scatterred than those obtained from simulations with clustered pores, and are of the order of a few percent of the average value: the accuracy of this average value is thus of the same order of magnitude. The dispersion for the clustered microstructures are larger (10–20% of the average values), but the range of variation of the results for a given microstructure only slightly overlap with those obtained with another microstructure. The qualitative comparison of the responses between microstructures is thus possible without bias. A more quantitative comparison might of course also be possible at the price of an increased size of the unit cell, containing more clusters, and of an increased number of realizations. More precisely, a systematic study of the variance of the results as a function of the size of the investigated domain would allow us to be more predictive (see Kanit et al. (2003) for a discussion on these aspects). Such investigations are left to further work.

3. Numerical simulations based on the Fast Fourier Transform

3.1. The FFT method

The effects of the inhomogeneous distribution of porosity on the nonlinear behavior of a material with a perfectly plastic matrix are studied by means of the numerical method based on the Fast Fourier Transform method introduced by Moulinec and Suquet (1994). This method was specifically developed to deal with complex (periodic) microstructures such as those simulated in Section 2 at a much lower computational cost than the finite element method. The FFT method is briefly described below; more details can be found in Moulinec and Suquet (1994, 1998), and in Michel et al. (2000).

The problem to be solved is the following. Let $w(x,\varepsilon)$ be the strain energy of the phases that compose an RVE V of the composite under consideration, subjected to the average strain E. The strains are infinitesimal and periodicity conditions are assumed at the boundary of the unit-cell. The local stress and strain fields obey the following equations:

$$\begin{cases} \operatorname{div}(\sigma(x)) = 0, & \sigma(x) = \frac{\partial w}{\partial \varepsilon}(x, \varepsilon(u)), \\ \varepsilon(u) = E + \varepsilon(u^*), & u^*\#, \sigma \cdot n - \# \end{cases} \tag{1}$$

where $u^*\#$, $\sigma\cdot n-\#$ denote a periodic fluctuating displacement u^* and an anti-periodic traction $\sigma\cdot n$, respectively. As proposed by Eshelby in his pioneering work (Eshelby, 1957), problem defined by Eq. (1) can be reformulated by introducing a homogeneous linear elastic reference medium with stiffness c_0 and a nonuniform polarization field $\tau(x)$:

$$\begin{cases} \operatorname{div}(\sigma(x)) = 0, & \sigma(x) = c_0 : \varepsilon(u(x)) + \tau(x), \\ \varepsilon(u) = E + \varepsilon(u^*), & u^*\#, \sigma \cdot n - \#, \end{cases} \tag{2}$$

where the polarization field $\tau(x)$ reads

$$\tau(x) = \frac{\partial w}{\partial \varepsilon}(x, \varepsilon(u)) - c_0 : \varepsilon(u(x)). \tag{3}$$

The solution of Eq. (2) can be expressed in Fourier space by means of the periodic Green operator Γ^0 associated with the reference medium with stiffness c_0

$$\hat{\varepsilon}(\xi) = -\widehat{\Gamma}^0(\xi) : \hat{\tau}(\xi) \quad \forall \xi \neq 0, \ \hat{\varepsilon}(0) = E. \tag{4}$$

In Eq. (4), $\hat{f}(\xi)$ stands for the Fourier transform of $f(x)$. Finally, due to the nonlinear dependence of the polarization field given by Eq. (3) on the local strain field, problem defined by Eq. (1) is equivalent to a nonlinear integral equation (which reduces to the well-known Lippmann–Schwinger equation when the composite is linear). In order to solve this nonlinear integral equation, Moulinec and Suquet (1998) have proposed a fixed-point method based on the iterative equation

$$\hat{\varepsilon}^{n+1}(\xi) = -\widehat{\Gamma}^0(\xi) : \hat{\tau}^n(\xi) \quad \forall \xi \neq 0, \qquad \hat{\varepsilon}^{n+1}(0) = E, \tag{5}$$

where

$$\tau^n(x) = (\partial w/\partial \varepsilon)(x, \varepsilon^n) - c_0 : \varepsilon^n(x).$$

In practice, the computation of $\hat{\tau}^n(\xi)$ requires the computation of $\tau^n(x)$ in real space and therefore a direct and an inverse Fourier transform to pass from one space to the other. A limitation of this fixed-point method is that convergence is directly related to the contrast between the phases. Convergence is therefore not ensured for composites with infinite contrast, which is precisely the case here for porous materials. To overcome this difficulty, a method based on an augmented Lagrangian has been proposed by Michel et al.

(2000). The resulting saddle-point problem is solved by means of a Uzawa algorithm which involves three steps. The first step consists in solving a homogeneous linear elastic problem with eigenstress similar to Eq. (2) and makes use of Eq. (4) in Fourier space. In the second step, a nonlinear problem is solved at each individual point in the RVE. The third step consists in updating the Lagrange multiplier and is also a local step in real space (see Michel et al., 2000; Michel et al., 2001 for more details).

3.2. Application to porous materials with a rigid perfectly-plastic matrix

As in Gurson's analysis, we will consider only rigid perfectly-plastic materials. In this case the material behavior derives from a strain energy (indeed a dissipation potential) which reads

$$w(x,\varepsilon) = \sigma_0 \varepsilon_{\mathrm{eq}}, \tag{6}$$

where σ_0 is the yield stress and $\varepsilon_{\mathrm{eq}}$ the equivalent strain (or strain-rate). Note that, in rigid perfect-plasticity, ε can be rigorously interpreted as a strain-rate.

For a rigid-plastic von Mises matrix, the nonlinear problem in the Uzawa algorithm described by Eq. (9) in Michel et al. (2000) is not smooth enough since the function $w(x,\varepsilon)$ cannot be differentiated at the origin. To overcome this difficulty, the energy function is regularized by adding an isotropic elastic term (Michel et al., 2000) in such a way that

$$w(x,\varepsilon) = \frac{9}{2} k \varepsilon_{\mathrm{m}}^2 + f(\varepsilon_{\mathrm{eq}}) \quad \text{with } f(\varepsilon_{\mathrm{eq}}) = \begin{cases} \frac{3}{2}\mu\varepsilon_{\mathrm{eq}}^2 + \frac{\sigma_0^2}{6\mu} & \text{when } \varepsilon_{\mathrm{eq}} \leqslant \frac{\sigma_0}{3\mu} \\ \sigma_0 \varepsilon_{\mathrm{eq}} & \text{when } \varepsilon_{\mathrm{eq}} \geqslant \frac{\sigma_0}{3\mu}, \end{cases} \tag{7}$$

where k and μ are the elastic bulk and shear moduli, respectively, and are chosen arbitrarily. The addition of the elastic term, which does not affect the yield surface of the porous material, is just a numerical artifice. This is only the case in the present framework of small strains: microstructure evolutions associated with finite strain elasticity, as considered by Tvergaard (1999), are out of the scope of the present work.

The determination of the yield surface requires a step-by-step procedure. The average strain E is applied incrementally as $E(t) = tE_0$, where E_0 is a prescribed strain direction. The evolution of the local strain and stress fields $\varepsilon(u(t,x))$ and $\sigma(t,x)$ solution of Eq. (1) is then computed. When t goes to infinity, the average stress $\Sigma(t) = \langle \sigma(t) \rangle$ stands on the yield surface of the porous material and E_0 is an outer normal to the yield surface at this point. The method can be modified to follow a prescribed direction in stress space. In this case, a mixed procedure is adopted in which the direction Σ_0 of the average stress is prescribed as $\Sigma(t) = k(t)\Sigma_0$ and the unknown amplitude $k(t)$ is determined from the condition $\Sigma_0 : E(t) = t$. The latter procedure leads to a more accurate determination of the yield surface (Michel et al., 1999).

The rate of convergence of the augmented Lagrangian method depends on the choice of a stiffness tensor c_0 which stands for the homogeneous reference medium. In the absence of theoretical arguments for the optimal choice of this tensor, it has been determined numerically. As mentioned in Michel et al. (2001), the choice of the optimal value of c_0 does not depend very strongly on the spatial resolution of the picture. In our simulations, the stiffness of the reference medium was given by $c_0 = 8c$, c being defined by k and μ.

For computational purposes, the images are discretized into 1215^2 pixels in two dimensions and 128^3 or 64^3 voxels in three dimensions. The three-dimensional discretization of 64^3 pixels, which may seem relatively coarse, proved to be sufficient: the results obtained on the same microstructure discretized into 64^3 voxels and into 128^3 voxels differ by less than one percent in terms of overall stress.

3.3. Overall loading conditions

Three-dimensional microstructures with very large unit cells are close to being isotropic, since the statistical process by which they were generated does not select any preferential direction. The effective behavior

should therefore only depend on the three invariants of the overall stress Σ, namely the mean stress $\Sigma_m = \mathrm{tr}(\Sigma)/3$, the equivalent von Mises stress $\Sigma_{eq} = \sqrt{\frac{3}{2}\mathrm{dev}(\Sigma) : \mathrm{dev}(\Sigma)}$, with $\mathrm{dev}(\Sigma)$ the deviatoric part of Σ, and the determinant $\det(\Sigma)$. The Gurson criterion and its variants depend explicitly on the two first invariants and have been developed for axisymmetric load conditions, by which the third invariant of the stress is completely determined by the first two invariants. In order to highlight the effects of the microstructure on the macroscopic behavior and to investigate the effect of the third invariant, nonaxisymmetric type-A loadings given by Eq. (8) in the frame (e_1, e_2, e_3) aligned with the periodicity directions, which combine pure shear with hydrostatic pressure, will be considered here in addition to more classical type-B loadings given by Eq. (9).

$$\Sigma = \begin{pmatrix} T & R & 0 \\ R & T & 0 \\ 0 & 0 & T \end{pmatrix}, \quad R > 0: \text{ Type-A loading.} \tag{8}$$

$$\Sigma = \begin{pmatrix} T & 0 & 0 \\ 0 & S & 0 \\ 0 & 0 & T \end{pmatrix}, \quad S > T: \text{ Type-B loading.} \tag{9}$$

Similar loading conditions will be considered for two-dimensional microstructures, with cylindrical voids aligned in the third direction and randomly distributed in the transverse plane, with or without clusters. Again, when the unit cell is very large, the overall behavior should be transversely isotropic, since the statistical process by which the position of the cylinders have been determined in the transverse plane does not select any preferential direction. The effective behavior depends then on the three above mentioned invariants and on two additional transversely isotropic invariants: the axial stress along the fibers, Σ_{33}, and the anti-plane shear $\Sigma^l_{eq} = \sqrt{\Sigma^2_{13} + \Sigma^2_{23}}$. The effect of the last invariant will not be investigated here. The dependence on Σ_{33} illustrates the fact that a type-B loading with fibers aligned in the third direction (i.e. a hydrostatic loading combined with a uniaxial tension in the transverse plane) differs from a type-B loading with the fibers aligned in the second direction (i.e. a hydrostatic loading combined with a uniaxial tension along the fibers), which is the condition considered by Gurson in his analysis of two-dimensional porous media. This last case has already been addressed by Michel et al. (2001) for random microstructures similar to those considered here and will not be discussed again here. In addition only positive mean stress will be investigated. The values of the five invariants for all loading conditions are summarized in Table 2.

Isotropy or transverse isotropy, which should be met exactly in the ideal case of an infinite cell, are hardly satisfied with unit cells of a finite size. However taking the ensemble averages of all computations performed over different realizations obtained with the same set of parameters defining the microstructure reduces the anisotropy induced by finite-size effects. All results will thus be interpreted as if they would exhibit the isotropy properties of large unit cells.

Table 2
Value of the invariants related to type-A, type-B and "2D-Gurson" type load

Load	Type-A	Type-B	"2D-Gurson"
Σ_m	T	$(2T+S)/3$	$(2T+S)/3$
Σ_{eq}	$\sqrt{3}R$	$S-T$	$S-T$
$\det(\Sigma)$	$T(T^2-R^2) = \Sigma_m(\Sigma_m^2 - \frac{1}{3}\Sigma_{eq}^2)$	$ST^2 = \left(\Sigma_m + \frac{2}{3}\Sigma_{eq}\right)\left(\Sigma_m - \frac{1}{3}\Sigma_{eq}\right)^2$	$ST^2 = \left(\Sigma_m + \frac{2}{3}\Sigma_{eq}\right)\left(\Sigma_m - \frac{1}{3}\Sigma_{eq}\right)^2$
Σ_{33}	$T = \Sigma_m$	$T = \Sigma_m^2 - \frac{1}{3}\Sigma_{eq}$	$S = \Sigma_m^2 + \frac{2}{3}\Sigma_{eq}$
Σ^l_{eq}	0	0	0

4. Two-dimensional computations

In the absence of anti-plane shear, i.e., $\Sigma_{13} = \Sigma_{23} = 0$, the translation invariance of the problem can be used to show that the displacement field solution of the three-dimensional problem corresponds to a generalized plane strain state:

$$u_\alpha = u_\alpha(x_1, x_2), \quad \alpha = 1, 2, \quad u_3 = E_{33} x_3, \tag{10}$$

where direction 3 is the fiber direction. The following two-dimensional calculations have been performed within this generalized plane strain framework. Therefore the two-dimensional microstructures correspond to voided materials containing aligned cylindrical voids and subjected to a macroscopic stress without anti-plane shear.

All FFT calculations presented in this section have been performed on microstructures similar to those shown in Figs. 3 and 4 of Section 2.

4.1. Yield stress

Consider first a purely hydrostatic loading ($R = 0$, type-A loading) and a pure in-plane shear loading ($T = 0$, type-A loading). The macroscopic stress–strain curves $\Sigma_m = f(E_m)$ and $\Sigma_{eq} = f(E_{eq})$, where E_m and E_{eq} are the macroscopic mean strain and the macroscopic equivalent strain respectively, are derived from a step by step procedure, as explained in (Michel et al., 1999). They are shown in Fig. 6.

The clustered microstructures can be considered as softer than the random ones. Among them, those with a connected cluster have a smaller yield stress than those with disconnected clusters. Hence, the pore spatial distribution can be considered as an important microstructural property of porous media. In general, the sensitivity of the overall yield stress with respect to the microstructure, quantified by its relative variation for the three types of microstructure, is larger (50%) for a hydrostatic loading than for a pure shear loading (10%). In Fig. 6, the error bars refer to the extreme values of the computed stress for the four statistical realizations which have been generated for each type of microstructure, to balance the relatively small size of the RVEs, whereas the solid or dashed lines correspond to the ensemble averages of the results. The dispersion of the results is expected to decrease as the RVE becomes larger, as discussed earlier, but it is already sufficiently small to clearly reveal the dependence of the effective behavior on the type of microstructure.

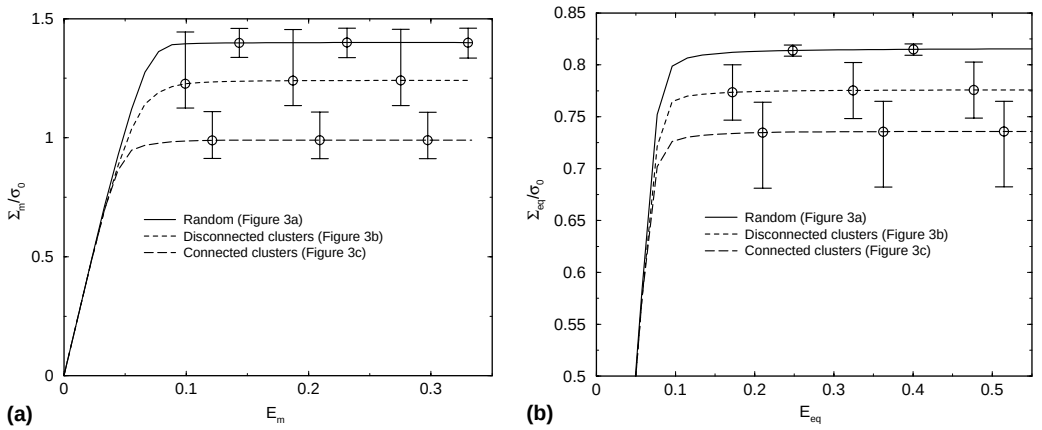

Fig. 6. Two-dimensional problems. Macroscopic yield stress: (a) hydrostatic macroscopic stress and (b) in-plane macroscopic shear.

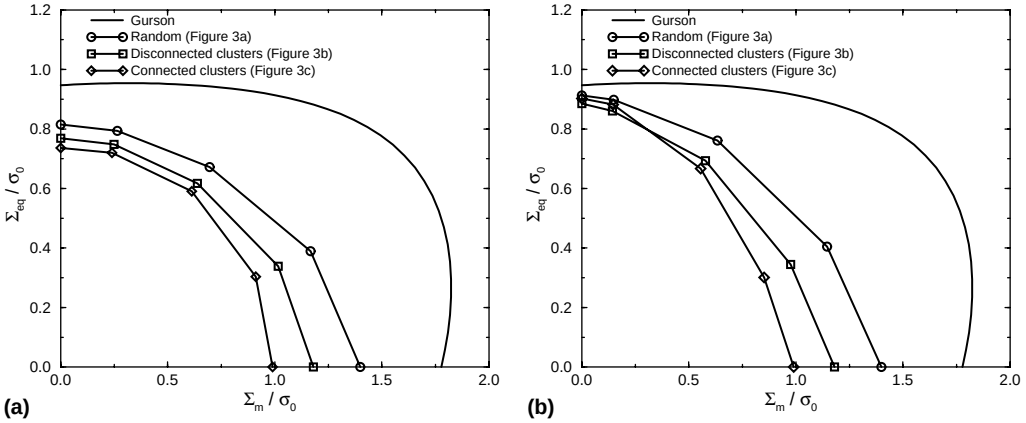

Fig. 7. Macroscopic yield surface: (a) type-A loading and (b) type-B loading.

An arbitrary type-A loading is now considered, varying from a purely hydrostatic stress to an in-plane shear. The corresponding yield surface can be represented in the plane (Σ_m, Σ_{eq}). Five different triaxiality ratios $\tau = \frac{\Sigma_m}{\Sigma_{eq}}$ were considered. For each of them and for each microstructure, the macroscopic yield stresses on the yield surface (Σ_m, Σ_{eq}) were determined by the FFT simulations. The results corresponding to microstructures with a single void size (see Fig. 3) are reported in Fig. 7.

The influence of the type of microstructure follows the same general trends as in the case of a purely hydrostatic stress or a pure shear: the weaker configurations are the connected clustered microstructures, the stronger configurations are the random configurations, whereas the disconnected clustered microstructures give intermediate results.

Two-dimensional FFT simulations have also been performed for type-B loadings. The associated results are also shown in Fig. 7b. The same hierarchical order as for type-A loadings between the different types of microstructure is observed except for purely deviatoric load where the dependence on the microstructure is small. One can also note that the computed yield stress for a given microstructure is *larger* than for type-A loadings except, of course, for a purely hydrostatic stress which is the same for both loadings.

The FFT results can be compared with the predictions of two-dimensional Gurson (1977), which has been derived for axisymmetric loads along the direction of the fibers, and reads

$$\left(\frac{\Sigma_{eq}}{\sigma_0}\right)^2 + 2f\cosh\left(\frac{\sqrt{3}}{2}\frac{\Sigma_{\alpha\alpha}}{\sigma_0}\right) - 1 - f^2 = 0, \text{ with } \Sigma_{\alpha\alpha} = \Sigma_{11} + \Sigma_{22}, \tag{11}$$

where f is the macroscopic porosity and σ_0 the matrix yield stress. As shown in Fig. 7, the Gurson model yields the stiffest response. This excessive stiffness follows from the fact that Gurson's model given by Eq. (11) is built on the assumption of full plastification of the matrix in the RVE and does not account for a possible strain localization between the pores as discussed in the following section. In addition the axisymmetric loading for which this criterion was designed is less susceptible of strain localization, at least for low triaxiality, as calculations by Michel et al. (2000) have shown. The type-A loading for which the deviatoric part of the stress only contains transverse shear components, may cause much stronger strain localization as shown in the next section. The type-B loading is intermediate, since its deviatoric part contains both a transverse shear part $\frac{T-S}{2}(e_2 \otimes e_2 - e_1 \otimes e_1)$ and an axial part $\frac{T-S}{3}(2e_3 \otimes e_3 - e_1 \otimes e_1 - e_2 \otimes e_2)$.

Finally, let us mention for completeness that results (not reported here) similar to those shown in Figs. 6 and 7 have been obtained for microstructures with a variable pore size (polydisperse case). For a given class

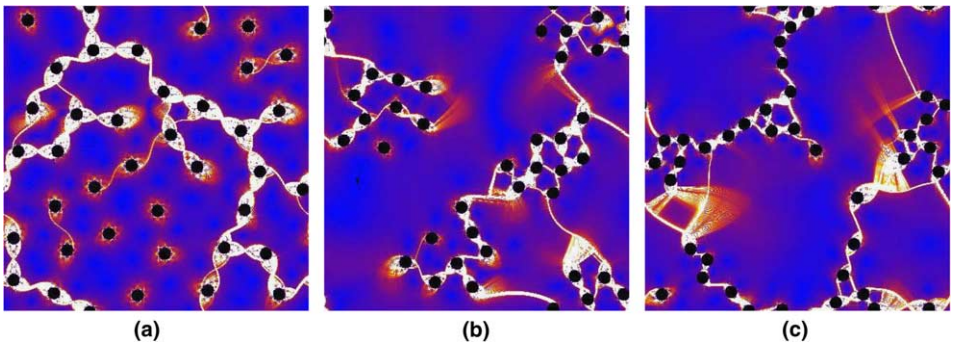

Fig. 8. Snapshot of the local equivalent strain for a purely hydrostatic macroscopic stress: (a) random microstructure (b) microstructure with disconnected clusters and (c) microstructure with a connected cluster.

of microstructure, it has been observed that voided materials with a single pore size (monodisperse) are stronger than voided materials with a variable pore size (polydisperse case not reported here).

4.2. Local fields

The equivalent strain fields for a purely hydrostatic and for a pure shear loading are shown in Figs. 8 and 9, respectively. In these snapshots and in the following ones, blue zones are almost not deformed, white areas are the more strained and red parts undergo intermediate deformations. The overall strain is such that the overall stress has reached a plateau. In both cases, the deformation tends to concentrate into bands. Under pure shear loading, the bands are almost straight and their orientation, horizontal and/or vertical, is governed by the overall loading. According to preliminary results of a study which is still in progress, bands go through planes where the pore density is maximum. Similar conclusions have already been drawn from an experimental study on two-phase materials by Bornert and Doumalin (2000). Under purely hydrostatic loading, the bands are more wavy and their position is determined by the local configuration of the pores since no preferential orientation is imposed by the loading.

This strain localization mode must be considered in parallel with the yield stress for the different types of microstructure: the easier the localization is, depending on the microstructure and the associated pore and cluster connectedness, the lower the overall yield stress. On the other hand, the larger the triaxiality ratio,

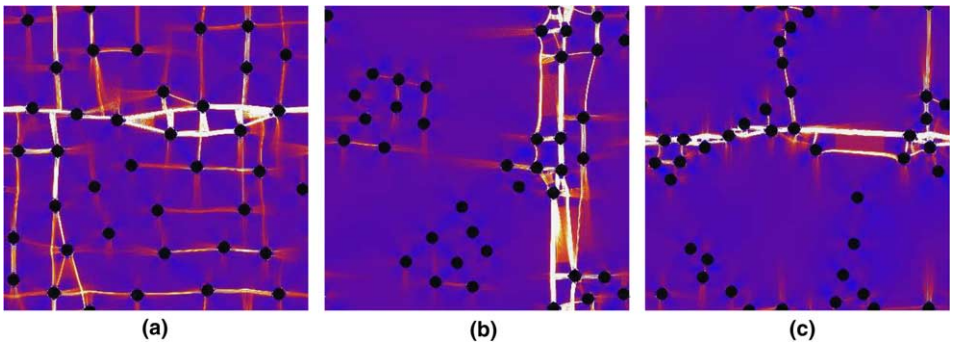

Fig. 9. Snapshot of the local equivalent strain for pure shear in the transverse plane: (a) random microstructure; (b) microstructure with disconnected clusters and (c) microstructure with a connected cluster.

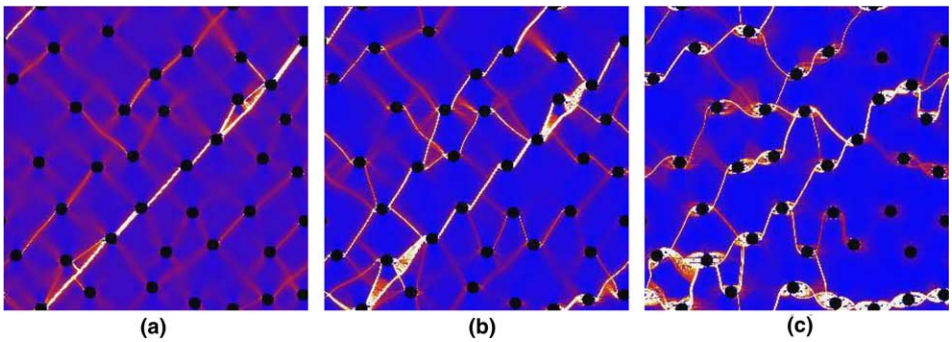

Fig. 10. Snapshot of the local equivalent strain for type-B loading and different triaxiality ratios: (a) $\tau = \frac{1}{3}$; (b) $\tau = 1$ and (c) $\tau = 3$.

the larger the band width and the more pronounced their spreading. The latter conclusion is illustrated in Fig. 10: when the triaxiality ratio is small, the orientation of the bands is fixed by the loading whereas, at larger triaxiality ratios, the orientation of the bands is more and more determined by the location of the pores. These properties are even more visible in the extreme cases of Figs. 8 and 9.

5. Three-dimensional computations

The microstructures used in the three-dimensional computations are shown in Fig. 5 of Section 2.

5.1. Yield stress

The dependence of the macroscopic mean stress Σ_m on the mean strain E_m for pure hydrostatic loading and of the equivalent stress Σ_{eq} on the equivalent strain E_{eq} for type-A and type-B loadings at zero triaxiality ratio ($\Sigma_m = 0$) is reported in Figs. 11 and 12, respectively. A spatial resolution of 128^3 voxels was used for these loading conditions. Five realizations were used in all calculations except in the case of microstruc-

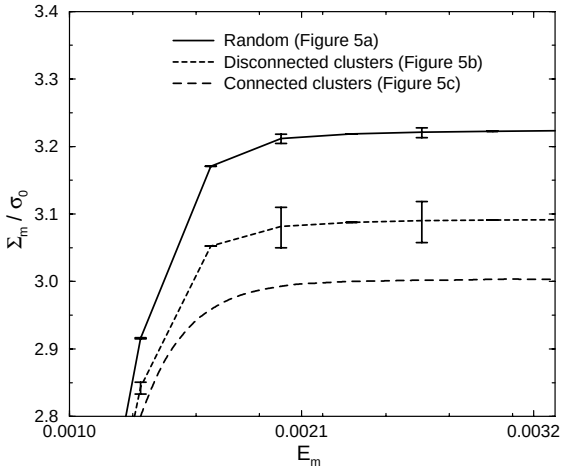

Fig. 11. Macroscopic yield stress for a purely hydrostatic load. Image resolution: 128^3 voxels.

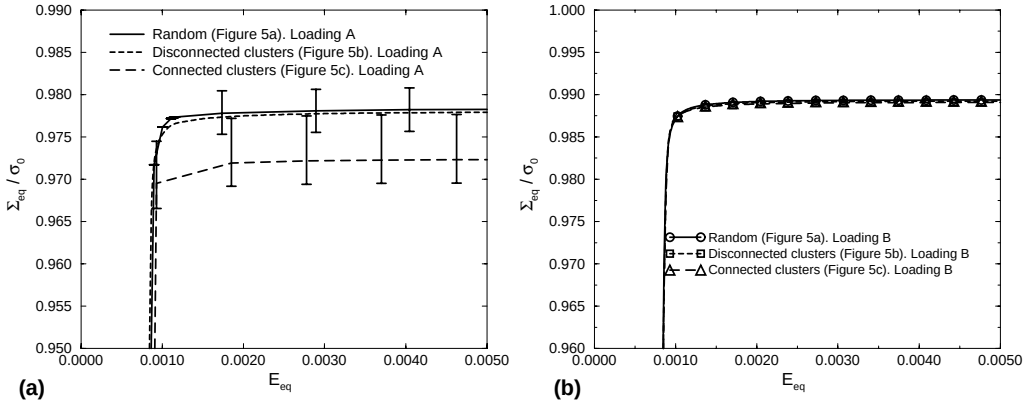

Fig. 12. Three-dimensional problem. Macroscopic yield stress at zero triaxiality ratio. Image resolution: 128^3 voxels: (a) type-A loading and (b) type-B loading.

tures with connected clusters, for which only one realization was used. The corresponding dispersion is again given on the plots, the error bars indicating the extreme values and the continuous line corresponding to the averages.

The same trends as in the two-dimensional case are observed in Fig. 11: the random microstructure is the strongest microstructure and the microstructure with a connected cluster is the weakest microstructure. In Fig. 12, the third stress invariant is shown to assess its influence on the macroscopic response, the first two invariants being the same for type-A and type-B loadings. In Fig. 12a, unlike the trends observed in Fig. 11, the yield stress associated with the connected cluster is almost as high as the one associated with random microstructures. The reason for that may probably be found in the fact that a significant dispersion of the computed yield stress—as already observed in Fig. 6—may occur and dominate the effect of the morphology at this small volume fraction (0.6% pores). For type-B loading, the dispersion observed in the case of random microstructures is too small to be seen on the curve : it is of the order of $10^{-4}\sigma_0$; it can be noted in addition that the different microstructures can hardly be distinguished for this loading condition, which suggests that pore distribution plays only a minor role in this case.

The yield surfaces (Σ_m, Σ_{eq}) are reported in Fig. 13 for both type-A and type-B loadings. The results of FFT calculations are compared with the predictions of various models such as the Gurson model and the Gurson–Tvergaard model which can be put in the form:

$$\left(\frac{\Sigma_{eq}}{\sigma_0}\right)^2 + 2qf\cosh\left(\frac{3}{2}\frac{\Sigma_m}{\sigma_0}\right) - 1 - (qf)^2 = 0,$$

where $q = 1$ in the original Gurson model and q varies from 1.25 to 1.5 in the Gurson–Tvergaard model.

Smaller cell sizes have been used for these calculations (64^3 voxels) with in general only one realization. Yield stresses for type-A loadings follow the same hierarchical order as in the two-dimensional case, except at low triaxiality ratios, where the dependence of the results on the morphology is small. For type-B loadings, the yield surface does not depend on the microstructure at small triaxiality ratios; the dependence is stronger at higher ratios and results similar to those obtained for type-A loadings are found for hydrostatic conditions. The third invariant of the stress is seen to play a significant role as illustrated in the zoom of Fig. 13c at small triaxiality ratios. For a discussion of this role, which was also observed for a periodic distribution of pores, the reader is referred to Richelsen and Tvergaard (1994) who have performed finite

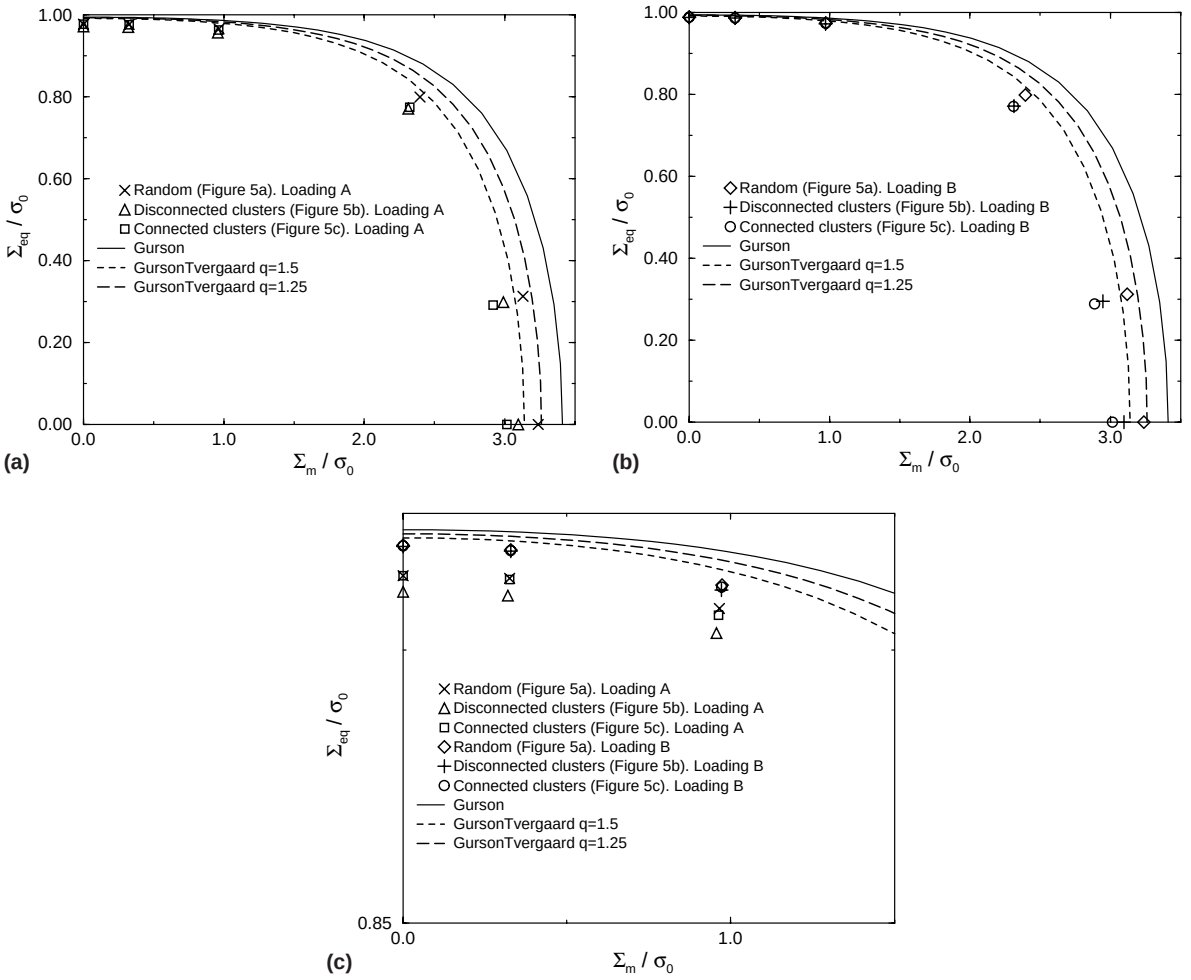

Fig. 13. Three-dimensional macroscopic yield surface. Comparison between the FFT calculations, Gurson's model, Gurson–Tvergaard's model Image resolution: 64^3 voxels (a) type-A loading; (b) type-B loading and (c) zoom for low triaxiality ratios.

elements simulations on a one pore unit cell. It should be noted that the Gurson and the Gurson–Tvergaard models overestimate the yield surface at all triaxiality ratios, and that the discrepancy is maximal at intermediate triaxiality ratios.

5.2. Local fields

The snapshot of the equivalent strain on a transverse cross-section of the RVE is shown in Fig. 14 for a purely hydrostatic loading. Once again, the deformation tends to localize into bands, especially in the case of the microstructure with a connected cluster. The band orientation is still imposed by the local pore configuration since no preferred orientation is associated with the applied load. The localization seems to be less pronounced for the microstructure with disconnected clusters. This is only due to the fact that it follows a three-dimensional path and is not only concentrated in the chosen cross-section. Note that the bands were narrower in the two-dimensional case.

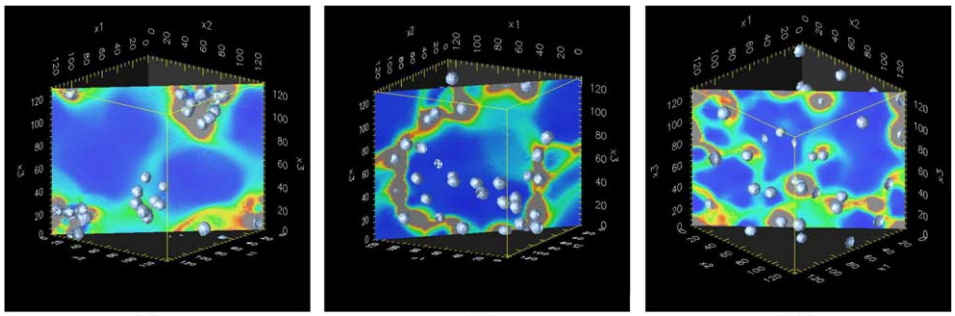

Fig. 14. Snapshot of the local equivalent strain for a purely hydrostatic load: (a) Microstructures with disconnected clusters; (b) microstructures with connected clusters and (c) random microstructure.

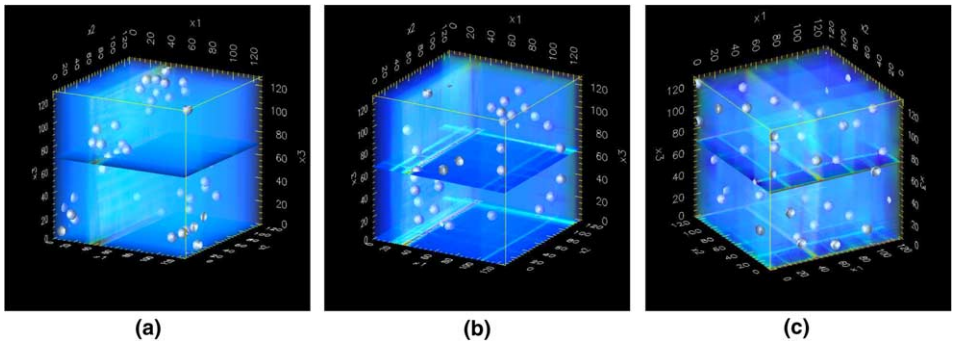

Fig. 15. Snapshot of the local equivalent strain for a pure in-plane shear load: (a) microstructure with disconnected clusters and (b) microstructure with connected clusters and (c) random microstructure.

Snapshots on successive cross-sections of the RVE of the local equivalent strain in the case of a pure shear type-A loading are shown in Fig. 15. The localization mode is almost planar. The planes are vertical and their orientations are determined by the applied loading as in the two-dimensional case. The number of localization planes is larger—and therefore the strain field is more diffuse—for the random microstructure than for the microstructures with clusters. Hence, the localization seems again to be more severe in the case of microstructures with connected or disconnected clusters than in the case of a random microstructure. Local fields for type-B loading are not reported here since no strong localization could be observed; the plastic flow seemed to be much more diffuse than for type-A loading. This may explain the small influence of the pore distribution on the overall behavior. Additional computation with enhanced resolutions are however necessary to confirm this tendency.

6. A statistical tool

It follows from the preceding sections that the plastic behavior of voided materials can be strongly influenced by details of their microstructure, such as the presence of clusters of voids. Moreover the nature of the clusters, connected or disconnected, matters. To detect the presence of clusters in a real microstructure, an image analysis tool is required. We propose here a statistical tool based on the distance function.

6.1. The distance function

The distance function from a point to a given set is the Euclidian distance from this point to the nearest element belonging to this set. When applied to the matrix of a porous medium, it gives the distance $d(x) = \min_j\{d^j(x)\}$ where $d^j(x)$ is the distance from any point x of the matrix, discretized into pixels or voxels, to the edge of the pore j. When all the pores j are circular or spherical, with radius r_j, a convenient normalized distance can be defined as the minimum ratio of $d^j(x)$ over r_j, namely

$$\hat{d}(x) = \min_j\left\{\frac{d^j(x)}{r_j}\right\}.$$

The distribution of such functions applied to the microstructures of Figs. 3 and 5 is plotted in Figs. 16 and 17. We recall that in these figures, the width of the unit cell has been taken to be 1.

The simulated two-dimensional microstructures of Fig. 3 were generated directly from two-dimensional processes. When real microstructures are investigated, the experimental data provide us only two dimen-

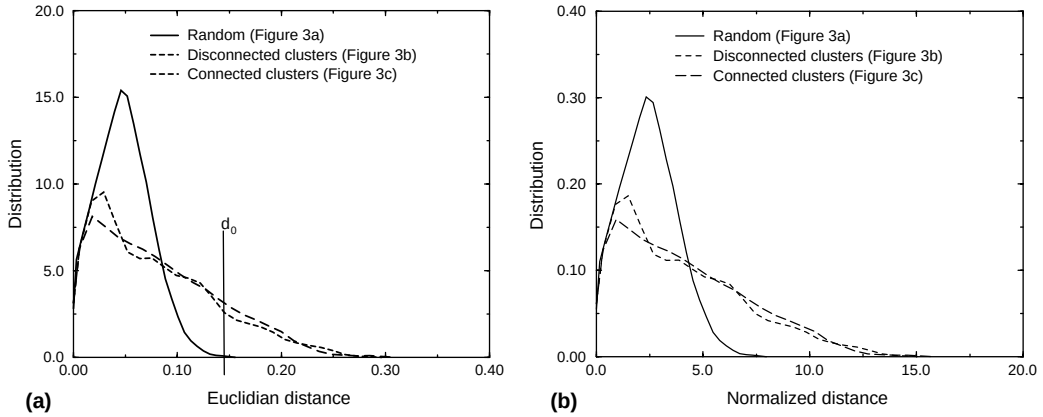

Fig. 16. Two-dimensional microstructures with single pore size: (a) distribution of the distance function and (b) distribution of the normalized distance function.

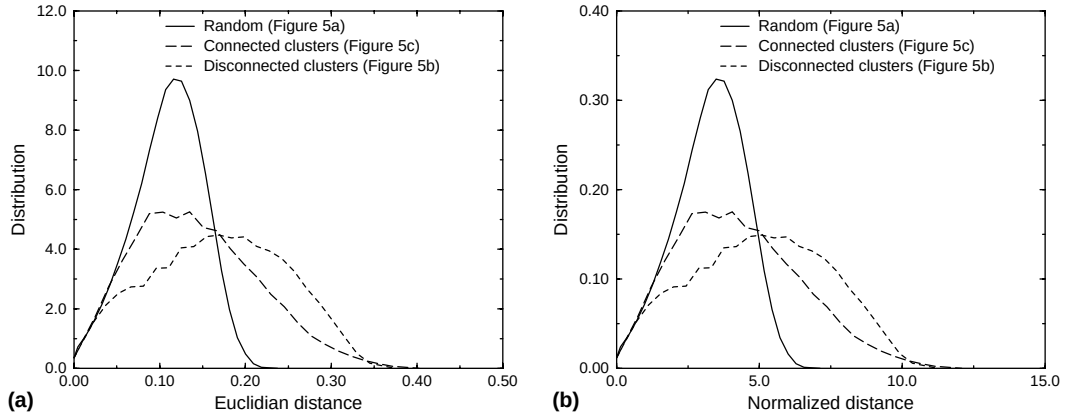

Fig. 17. Three-dimensional microstructures with single pore size (Fig. 5): (a) distance function and (b) normalized distance function.

sional pictures. If two-dimensional simulations are then performed for comparison, the corresponding microstructures can be either simulated directly from two-dimensional processes or obtained as two-dimensional cross-sections of three-dimensional microstructures. Obviously, the resulting two-dimensional statistical properties will be different.

Figs. 16 and 17 show that the distribution of the distance function exhibits some sensitivity to the class of microstructure and can at least be used for comparison. In addition, they suggest that the width of the distribution of the distance function is larger for clustered microstructures than for random ones. For the sake of clarity, only microstructures with a single pore size have been reported in Figs. 16 and 17. However, similar results have been obtained for microstructures with a variable pore size. Therefore, both the distance function and the normalized distance function could be used to detect the presence of clusters. However, both of them are unable to distinguish connected from disconnected clustered microstructures. So, additional statistical tools are needed.

6.2. Connectedness analysis

To go further in the analysis, a threshold distance d_0 is introduced (see Fig. 16a). For each value of d_0, the set of the matrix points with a distance to the nearest pore less than d_0 is determined (displayed in gray in Fig. 18 from a binary image of the RVE) and the number of connected components of this grey set is counted. The associated two-dimensional graph, where the number of connected components is plotted as a function of d_0 (see Fig. 19) can be used to distinguish between connected and disconnected clustered microstructures.

When d_0 is small, the number of gray zones is maximum and coincides with the total number of pores inside the RVE. When d_0 increases, the number of connected components decreases because of the progressive overlap of gray zones. This occurs much earlier for clustered microstructures than for random ones. The presence of well-separated inner characteristic scales for the system under study is associated with plateaus on the plots. Especially, when a characteristic size of disconnected clusters exists, there exists a specific value of d_0 representative of this size around which the curve exhibits a first plateau. The height of the plateau measures the number of isolated clusters and this plateau occurs only for this type of microstructure. In this way, disconnected clustered microstructures can be distinguished from connected clustered ones (as well as from random microstructures). For very large values of d_0, all the curves converge towards a last plateau which expresses the fact that there remains only one grey zone. This scheme can also be applied to three-dimensional microstructures as shown in Fig. 20 associated with the microstructures of Fig. 5. The experimental determination of the three-dimensional position of the pores might be a problem, since

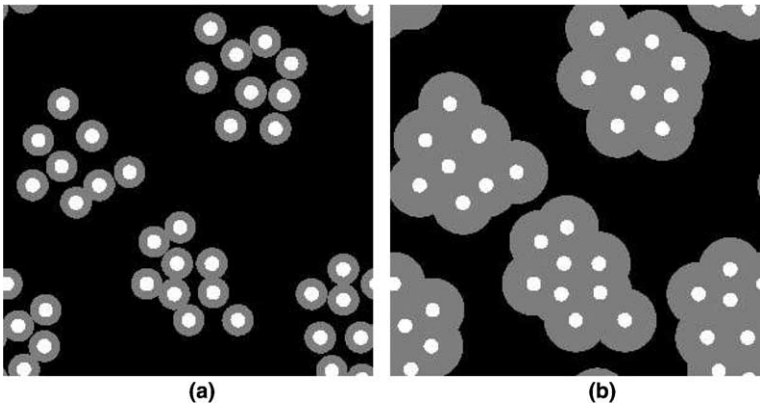

Fig. 18. Result of the threshold operation performed on the distance function: (a) $d_0 = 0.023$ and (b) $d_0 = 0.066$.

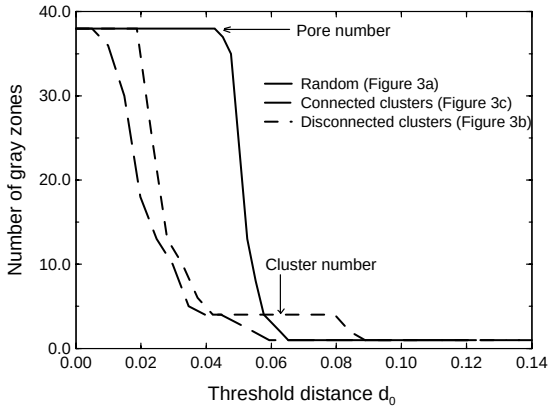

Fig. 19. Number of connected elements (i.e., of independent grey zones) as a function of the threshold distance d_0 for two-dimensional microstructures with constant void size (Fig. 3).

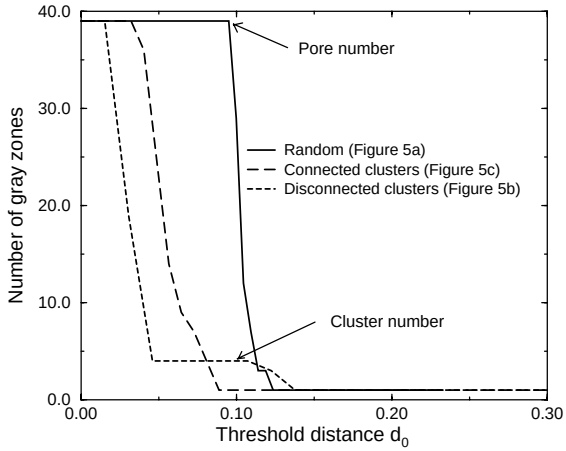

Fig. 20. Number of connected elements (i.e., of independent grey zones) as a function of the threshold distance d_0 for three-dimensional microstructures with constant void size (Fig. 5).

two-dimensional sections are no longer sufficient. Modern tools such as microtomography might however be used to overcome this difficulty.

The sensitivity of this method has been checked by use of five realizations for each type of microstructure. The results show a rather small variation of the distance function from one realization to another. The same conclusion holds for the connectedness analysis. More precisely, when the microstructures are of the cherry pit type (i.e., when a minimal distance is imposed between neighboring voids and clusters), the differences are really negligible. They increase slightly when the hard sphere model is used: since this minimal distance vanishes, the variability of the void distribution is larger and some slight fluctuations can be observed.

7. Conclusion

Numerical simulations based on the Fast Fourier Transform have been performed on microstructures made of perfectly plastic porous media containing different void distributions. They show a significant

influence of the void distribution on the overall yield properties and on the local mechanical fields. The stiffest responses correspond to random microstructures with no particular void clusters. The softest responses correspond to microstructures with a connected cluster of voids. The responses for microstructures containing isolated clusters of voids lie in between the two preceding cases. From the above reported results and from other simulations that have not been presented here for brevity, it follows that, for a given porosity and a given class of microstructure, the response seems to be softer when the void size is variable than when it is constant. These macroscopic effects are enhanced when the overall stress triaxiality is large.

At the local scale, the strain fields exhibit a pronounced localization into narrow bands whose activity and patterns depend on the class of microstructure: these bands are more easily observed in the case of clustered microstructures with connected cluster under pure overall shear. When clusters are present, the bands are straighter. Their orientation is mainly governed by the overall stress but their location is dependent on the microstructure: they seem to choose paths of maximal void density. When the loading is close to purely hydrostatic conditions, the two-dimensional bands are more curved and spread.

These phenomena are expected to play a significant role on the fracture behavior of industrial metals and alloys, where inclusions can behave as initial voids: this is being investigated both theoretically and experimentally in a study of the brittle–ductile transition of nuclear steels (Bilger, 2003).

References

Becker, R., 1987. The effect of porosity distribution on ductile failure. J. Mech. Phys. Solids 35, 577–599.

Benzerga, A., Besson, J., Pineau, A., 1999. Coalescence-controlled anisotropic ductile fracture. J. Eng. Mater. Technol. 121, 221–229.

Bilger, N., 2003. A micromechanical analysis of the role of particle clustering on the brittle–ductile transition in nuclear steels. Ph.D. Thesis, Ecole Polytechnique, Palaiseau (France), October 2003 (in French).

Böhm, H.J., Rammerstorfer, F.G., 1995. Influence of the micro-arrangement on matrix and fiber damage in constinuously reinforced mmcs. In: Pineau, A., Zaoui, A. (Eds.), Micromechanics of Plasticity and Damage of Multiphase Materials. Kluwer, Dordrecht, pp. 19–26.

Bornert, M., Doumalin P., 2000. Computational and experimental investigations of the local strain field in elastoplastic two-phase materials. In: Miannay, D., et al, (Eds). EUROMAT 2000, Advances in Mechanical Behaviour, Plasticity and Damage, vol. 1, pp. 323–328.

Brockenbrough, S., Suresh, D., Wienecke, S., 1991. Deformation of metal–matrix composites with continuous fibers: geometrical effects of fiber distribution and shape. Acta Metall. Mater. 39 (5), 735–752.

Eshelby, J.D., 1957. The determination of the elastic field of an ellipsoidal inclusion, and related problems. Proc. R. Soc. London A 241, 376–396.

Faleskog, J., Shih, C.F., 1997. Micromechanics of coalescence—I. Synergistic effects of elasticity, plastic yielding and multi-size scale voids. J. Mech. Phys. Solids 45 (1), 21–50.

Gărăjeu, M., Suquet, P., 1997. Effective properties of porous ideally plastic or viscoplastic materials containing rigid particles. J. Mech. Phys. Solids 45, 873–902.

Gologanu, M., Leblond, J.-B., Devaux, J., 1993. Approximate models for ductile metals containing non-spherical voids—case of axisymmetric prolate ellipsoidal cavities. J. Mech. Phys. Solids 41 (11), 1723–1754.

Gurson, A.L., 1977. Continuum theory of ductile rupture by void nucleation and growth: Part I—yield criteria and flow rules for porous ductile media. J. Eng. Mater. Technol. 99, 1–15.

Kanit, T., Forest, S., Galliet, I., Mounoury, V., Jeulin, D., 2003. Determination of the size of the representative volume element for random composites: statistical and numerical approach. Int. J. Solids Struct. 40, 3647–3679.

Koplik, J., Needleman, A., 1988. Void growth and coalescence in porous plastic solids. Int. J. Solids Struct. 24, 835–853.

Leblond, J.B., Perrin, G., 1999. A self-consistent approach to coalescence of cavities in inhomogeneously voided ductile solids. J. Mech. Phys. Solids 47, 1823–1841.

Michel, J.-C., Moulinec, H., Suquet, P., 1999. Effective properties of composites materials with periodic microstructure: a computational approach. Comput. Methods Appl. Mech. Eng. 172, 109–143.

Michel, J.-C., Moulinec, H., Suquet, P., 2000. A computational method based on augmented lagrangians and fast fourier transforms for composites with high contrast. Comput. Model. Eng. Sci. 1 (2), 9–88.

Michel, J.-C., Moulinec, H., Suquet, P., 2001. A computational scheme for linear and nonlinear composites with arbitrary phase contrast. Int. J. Numer. Methods Eng. 52, 139–160.

Moulinec, H., Suquet, P., 1994. A fast numerical method for computing the linear and the nonlinear mechanical properties of composites. C. R. Acad. Sci. Paris II 318, 1417–1423.

Moulinec, Suquet, P., 1998. A numerical method for computing the overall response of nonlinear composites with complexes microstructures. Comput. Methods Appl. Mech. Eng. 157, 69–94.

Pardoen, T., Hutchinson, J.W., 2003. Micromechanics-based model for trends in toughness of ductile metals. Acta. Metall. Mater. 51, 133–148.

Perrin, G., Leblond, J.B., 1990. Analytical study of a hollow sphere made of plastic porous material and subjected to hydrostatic tension - Application to some problems in ductile fracture of metals. Int. J. Plast. 6, 677–699.

Pijnenburg, K.G.W., Van der giessen, E., 2001. Macroscopic yield in cavitated polymer blends. Int. J. Solids. Struct. 38, 3575–3598.

Richelsen, A.B., Tvergaard, V., 1994. Dilatant plasticity for upper bound estimates for porous ductile solids. Acta. Metall. Mater. 42 (8), 2561–2577.

Soppa, E., Schmauder, S., Fischer, G., 1998. Numerical and experimental investigations of the influence of particle alignment on shear band formation in Al/Sic. In: Carstensen, J.V., Leffer, T., Lorentzen, T., Pedersen, O.B., Sorensen, B.F., Winther, G. (Eds.), 19th Risö International Symposium on Material Science, pp. 499–504.

Thomason, P.F., 1990. Ductile Fracture of Metals. Pergamon Press, New York.

Torquato, S., 2003. Random Heterogeneous Materials. Springer-Verlag, Berlin.

Tvergaard, V., 1990. Material failure by void growth to coalescence. In: Hutchinson, J.W., Wu, T.Y. (Eds.), Advances in Applied Mechanics, vol. 27. Academic Press, New-York, pp. 83–151.

Tvergaard, V., 1999. Effect of large elastic strains on cavitation instability predictions for elastic-plastic solids. Int. J. Solids Struct. 36, 5453–5466.

Tvergaard, V., Niordson, C., 2004. Nonlocal plasticity effects on interaction of different size voids. Int. J. Solids Struct. 20, 107–120.